TUDelft

Delft University of Technology

Calibration-free estimation of field-dependent aberrations for single-molecule localization microscopy across large fields of view

Droste, Isabel; Schuitema, Erik; Khan, Sajjad A.; Hensgens, Myron; Heldens, Stijn; Smith, Carlas S.; van Werkhoven, Ben; Geertsema, Hylkje; Lidke, Keith A.; Stallinga, Sjoerd

Important note
To cite this publication, please use the final published version (if applicable).
Please check the document version above.

OPTICA

Calibration-free estimation of field-dependent aberrations for single-molecule localization microscopy across large fields of view

Isabel Droste,[1] Erik Schuitema,[2] Sajjad A. Khan,[3,4] Myron Hensgens,[1]
Stijn Heldens,[5] Carlas S. Smith,[6] Ben van Werkhoven,[7] Hylkje Geertsema,[1]
Keith A. Lidke,[3] Sjoerd Stallinga,[1,8,†] and Bernd Rieger[1,†,*]

[1]*Department of Imaging Physics, Delft University of Technology, Delft, The Netherlands*
[2]*ESSD Software Engineering, Rotterdam, The Netherlands*
[3]*Department of Physics and Astronomy, University of New Mexico, Albuquerque, New Mexico 87106, USA*
[4]*Nanoscience and Microsystems Engineering, University of New Mexico, Albuquerque, New Mexico 87106, USA*
[5]*Netherlands eScience Center, Amsterdam, The Netherlands*
[6]*Delft Center for Systems and Control, Delft University of Technology, Delft, The Netherlands*
[7]*Leiden Institute of Advanced Computer Science, Leiden, The Netherlands*
[8]*s.stallinga@tudelft.nl*
[†]*These authors contributed equally to this work.*
[*]*b.rieger@tudelft.nl*

Image quality in single-molecule localization microscopy depends largely on the accuracy and precision of the localizations. While under ideal imaging conditions, the theoretically obtainable precision and accuracy are achieved; in practice, this changes if (field-dependent) aberrations are present. Currently, there is no simple way to measure and incorporate these aberrations into the point-spread function (PSF) fitting; therefore, the aberrations are often taken as constant or neglected altogether. Here we introduce a model-based approach to estimate the field-dependent aberration directly from single-molecule data without a calibration step. This is made possible by using nodal aberration theory to incorporate the field dependency of aberrations into our fully vectorial PSF model. This results in a limited set of aberration fit parameters that can be extracted from the raw frames without a bead calibration measurement, also in retrospect. The software implementation is computationally efficient, enabling the fitting of a full 2D or 3D dataset within a few minutes. We demonstrate our method on 2D and 3D localization data of microtubuli, nuclear pore complexes, and nuclear lamina over fields of view of up to 180 μm and compare it with Gaussian fitting, spline-based fitting, and a deep-learning-based approach.

1. INTRODUCTION

Single-molecule localization microscopy (SMLM) [1–4] enables routine imaging at the nanoscale. The need for high throughput and much data implies that a large field of view (FOV) must be imaged, which is enabled by modern sCMOS sensors that have up to 10 Mpixels and by advanced illumination schemes [5–12]. A key problem that arises is that aberrations depend on the position in the FOV. This is problematic for both the precision and accuracy of in-plane (xy) localization, but even more so for 3D (xyz) localization. Up to now, aberrations, let alone field-dependent aberrations, are rarely considered in SMLM, as it is time-consuming and cumbersome to (i) measure them and (ii) include them in the fitting. For that reason, the default method for estimating the positions of the emitters is to fit a simplified point-spread function (PSF) model

to the recorded data. Typically, this simplified model is a Gaussian [13], which reduces the computational load to estimate the positions of millions of emitters to reconstruct a super-resolution image. Known drawbacks, however, are position biases in the case of asymmetric aberrations and of emitters with partially fixed orientation [14] and an underestimation of the photon count [15]. An alternative to the data-driven PSF model is the spline model [16], which requires calibration of the PSF by beads, potentially at various field and depth positions. Advantageously, a physically correct, fully vectorial PSF model could be used, so that high NA and polarization effects are properly considered. Moreover, field-dependent aberrations of the microscope can then automatically be incorporated, and emission dipole orientation as well, if needed.

Up to now such a full vectorial model is not used in practice for SMLM due to the computational load [17].

The current practical standard to measure field-dependent aberrations is a calibration in the form of an axial scan of many fluorescent beads distributed over the whole FOV [16–18]. Nanohole arrays have been tried as calibration samples as well [19]. An alternative is provided by the localization data itself, as millions of localization events are in fact millions of measurements of the microscope's PSF across the FOV. The localization data itself thus provide a wealth of information on the optical system, and the challenge is to unlock that information. The key obstacle is that each individual localization event does not allow for the fitting of aberration parameters next to the position, photon count, and background, because the data are much too noisy for a robust estimation of many parameters. Previously, Xu *et al.* applied pupil phase retrieval to an averaged set of 3D localization data, but only so using an approximate scalar PSF model and for global aberrations independent of the position in the FOV [20]. Recently, Liu *et al.* proposed a framework for inverse PSF modeling, enabled by automatic differentiation, and showed its applicability to vectorial PSF fitting of 3D localization datasets with field-dependent aberrations [21]. Here, we present an alternative method to estimate field-dependent aberrations from 2D or 3D single-molecule images alone, without any calibration measurement. We make this possible by fitting the localization data with a global optical aberration model, with a limited number of fit parameters, instead of fitting the full aberration content of each measured PSF separately. This global aberration model is derived from the so-called nodal aberration theory (NAT) [22], which provides explicit relations of the field dependency of the appearing aberration coefficients via low-order polynomials of the field coordinates. This eliminates the need for *ad hoc* smoothing of field-dependent aberrations as done in the inverse PSF modeling approach and enables application to 2D localization data.

2. SINGLE-MOLECULE LOCALIZATION WITH FIELD-DEPENDENT ABERRATIONS

Aberrations can be modeled by expressing the phase aberration function in the pupil plane in terms of Zernike modes. Using NAT, the Zernike coefficients A_{nm} can be expressed as low-order polynomials of the field coordinates (x, y) (see Section 2 in Supplement 1 for theory):

$$A_{nm}(x, y) = \sum_{l,q} \gamma_{lqnm} Q_{lq}(x, y),$$

where γ_{lqnm} are NAT coefficients, and $Q_{lq}(x, y)$ are products of (Legendre) polynomials of order l and q. We adapted NAT to the square shape of the FOV by using Legendre polynomials to
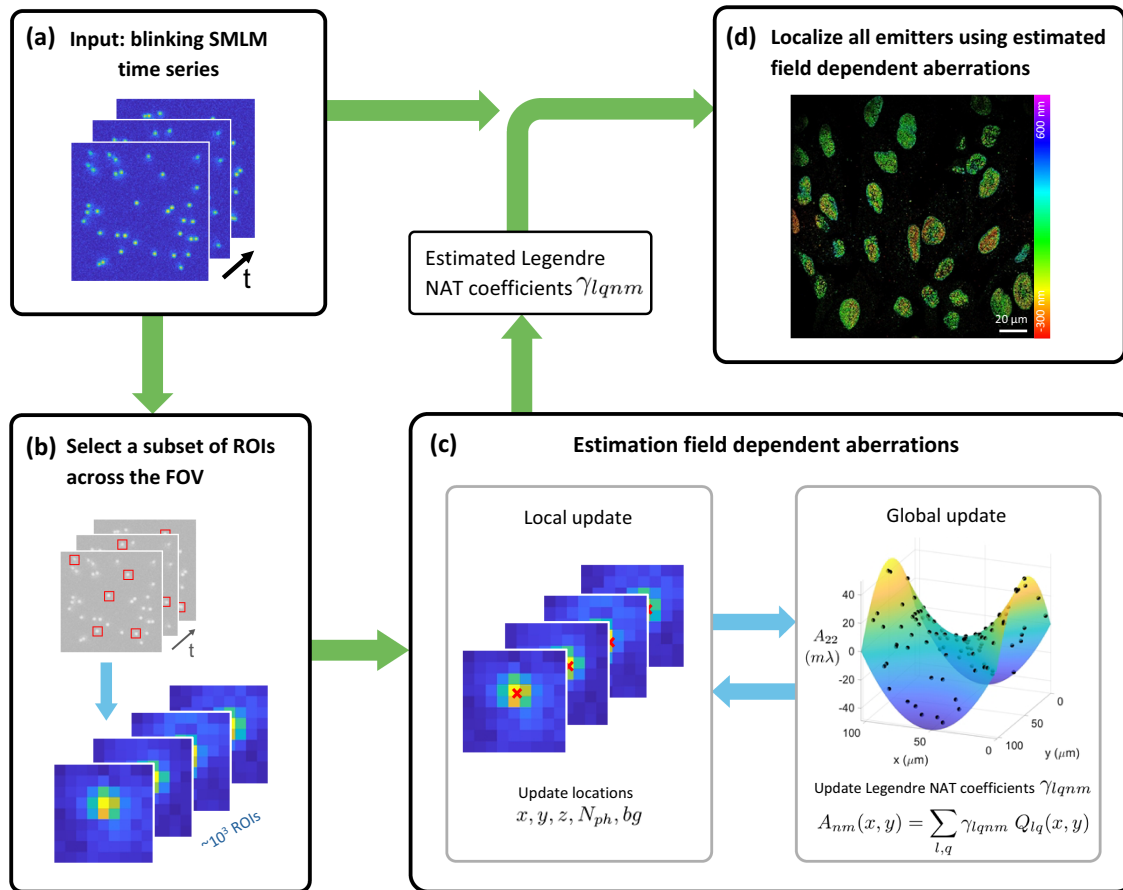

Fig. 1. Schematic of fitting field-dependent aberrations from single-molecule data. (a) The raw single-molecule blinking frames are used as input. (b) After segmentation into ROIs, a subset of $\sim 10^3$ ROIs across the FOV is selected for field-dependent aberration estimation. (c) The estimation of field-dependent aberrations uses maximum likelihood estimation and consists of two optimization loops: a local update that updates the locations, photon count, and background of each ROI while keeping the NAT coefficients constant, and a global update that updates the Legendre NAT coefficients while keeping the locations, photon count, and background constant. By selecting different ROIs in (b) multiple times and repeating the estimation (c), an estimation precision for the aberrations can be calculated. (d) Finally, in all ROIs, emitters are localized using the vectorial PSF model [24] with the estimated NAT coefficients as input.

describe the field dependence. For describing the field dependency of the first-order aberrations, that is, defocus, primary astigmatism, coma, and spherical aberration, it turns out that only 13 NAT coefficients are needed. To include second-order aberrations (trefoil and secondary astigmatism, coma, and spherical aberration), an additional 43 NAT coefficients are needed. This number of free parameters, though large, is still orders of magnitude less than the number of free parameters in data-driven approaches [16,23].

Figure 1 schematically depicts our method. The raw blinking time series data are segmented into regions of interest (ROIs) containing fluorescent emitters as usual for SMLM. From these millions of ROIs, a very small subset of $M_s \sim 10^3$ ROIs across the FOV is randomly selected to be used as input for the field-dependent aberration estimation. The estimation process consists of an alternation of local and global updates. During a global update, the NAT coefficients are updated while keeping the locations, photon count, and local background of the emitters fixed, while during a local update, the locations are updated with fixed NAT coefficients. Subsequently, all ROIs are fitted with a vector PSF model, "Vectorfit" for short [24], using the found field-dependent aberrations as input. We have implemented the vector PSF fitting on a GPU for speedup and have devised several algorithmic improvements for additional steps in efficiency. First, we utilize the phasor method to provide a fast, initial estimate of the lateral position that is robust against high background [25]. Second, we compute the initial estimate of photon count N_{ph} and background count bg with linear regression given the data and the model. Third, precomputing the optical transfer function (OTF) reduces the number of needed Fourier transformations per iteration by a factor of 6. These different algorithmic innovations are outlined in Section 1 in Supplement 1.

3. EXPERIMENTAL RESULTS

We have tested our method on SMLM data of microtubuli acquired over a large $97 \times 97\,\mu\mathrm{m}$ FOV (see Section 1 in Supplement 1 for experimental details). The same sample was imaged with and without astigmatism to obtain 2D and 3D localization data, respectively (see Fig. 2). The aberrations found from the single molecule data via our method give very similar aberration maps across the FOV [orange in Figs. 2(a) and 2(e)] as the aberration maps obtained by interpolating between aberrations retrieved from z-stack bead calibration data [light blue in Figs. 2(a) and 2(e)], with the largest difference in the slope of the coma aberration maps (see Figure S1 in Supplement 1 for the difference maps). We performed a chi-square goodness-of-fit test [26] to check whether the PSF model with single-molecule-derived aberrations gives rise to a better fit than the PSF model with bead-calibration-derived aberrations (Figure S2 in Supplement 1). For both the 2D and 3D data, we find on average about 1% smaller chi-square values for the single-molecule-derived aberrations, up to about 5% and 3% smaller at the edges of the FOV for the 2D and 3D datasets, respectively, indicating a slightly better fit of the single-molecule-derived aberrations. The overall chi-square values are about 20% (2D) and 16% (3D) higher than the theoretical values based on shot noise statistics [26] (Figure S3 in Supplement 1), indicating a residual model mismatch, possibly due to higher-order aberrations and amplitude aberrations. A further validation of our approach is found by a comparison of the modeled PSF to the measured single-molecule spots in 4×4 patches across the FOV, as a function of the

axial position (Visualization 1). This comparison shows that the modeled PSF matches very well with the measured data.

We also found a difference in the estimated bead aberrations between consecutive days of measurement with different bead samples. The beads measured on the second day show a uniform shift in the coma coefficient A_{3-1} (Figure S4 in Supplement 1). By estimating the z locations of the beads, we found that the tilt of the sample was different between the two measurement instances, most likely caused by remounting of a different bead sample on the stage. We attribute the difference in the estimated coma to this sample tilt, as passing a high NA emission beam through a tilted medium leads to coma that is constant over the FOV. Apparently, the aberration estimation from bead calibration data can be affected by small changes in the imaging conditions, like the sample tilt. Similar differences in imaging conditions can potentially arise between the bead calibration measurement and the actual single-molecule data acquisition, implying that estimation of aberrations from the data itself not only makes the bead calibration measurement spurious, but is also inherently more reliable.

We also used the chi-square goodness-of-fit test to assess the added value of taking the field dependency of the aberrations into account. We applied Vectorfit with all the aberrations set to zero, except for a constant amount of astigmatism ($A_{2-2} = 87$ mλ, equal to the average amount over the FOV estimated from the bead calibration) for estimating the axial location for the 3D data. Figure S3 in Supplement 1 shows that the PSF model with single-molecule data-derived field-dependent aberrations fits the data better than the model without aberrations, especially toward the edges of the FOV. A comparison of the estimated locations using the two models shows that the location difference increases with the distance from the center of the FOV (Figure S3d in Supplement 1). Moreover, for the 3D data, the shift in location is different for emitters with $z < 0$ than for emitters with $z > 0$ (Figure S3f in Supplement 1), which could lead to a distortion of the imaged structures when field-dependent aberrations are not considered.

We compared our reconstructions to existing methods, namely Picasso [27] for the 2D data and SMAP [28] for the 3D data (Visualization 3). Picasso uses a Gaussian PSF model where the horizontal and vertical standard deviations σ_x and σ_y are estimated for each ROI [13], whereas SMAP uses a spline PSF model that is uniform across the FOV, with parameters estimated from the experimental bead data. Figures 2(c) and 2(d) show that 2D reconstructions with Picasso are very similar to reconstructions with Vectorfit. The average localization precision, estimated by linking localizations in consecutive frames [29], is 10.0 nm for Vectorfit with a CRLB of 9.3 nm, better than the value of 13.5 nm found for Picasso with a CRLB of 14.2 nm. Figures 2(g)–2(j) show that 3D reconstructions with SMAP are similar to reconstructions with Vectorfit, where Vectorfit shows a somewhat smaller axial spread of the localizations. The linking analysis gives here an average localization precision of 12.1 nm (xy) and 29.9 nm (z), with a CRLB of 12.1 nm (xy) and 31.1 nm (z), compared to a precision of 12.1 nm (xy) and 35.7 nm (z) for SMAP. FRC image resolution [30] estimation (Figs. S5 and S6 in Supplement 1) shows a comparable performance between Vectorfit and the other software used.

An often used benchmark for SMLM is the nuclear pore complex (NPC) [31]. Specifically, the ability to show the nuclear and cytoplasmic ring of the NPC, separated only by ∼50 nm, is a hallmark of axial accuracy. We applied Vectorfit to such a 3D NPC
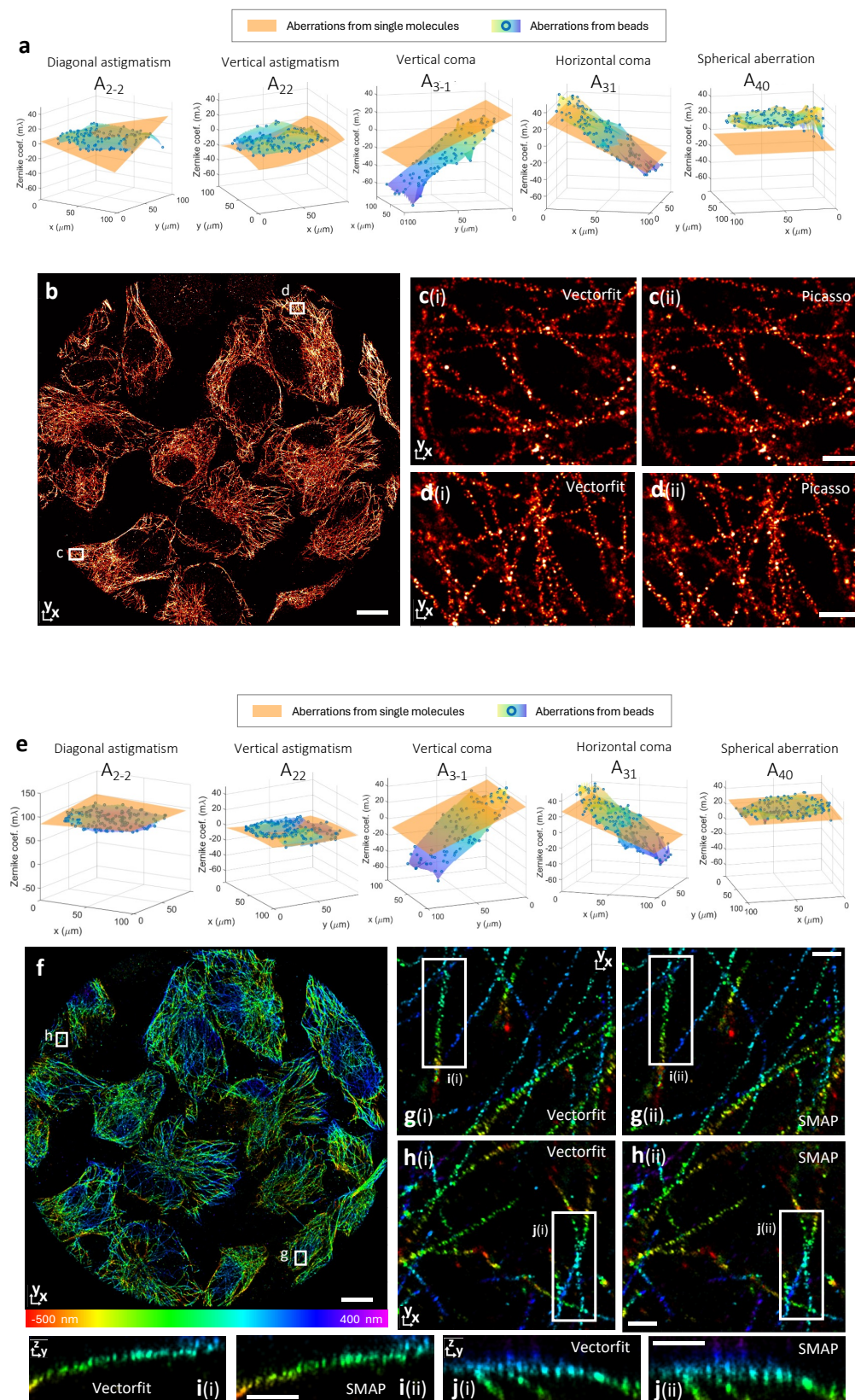
Fig. 2. Aberration estimation from 2D and 3D experimental data of microtubili. A sample was imaged in 3D with and in 2D without astigmatism. (a) Estimated Zernike aberration surfaces from single molecules of the 2D data, compared to interpolated aberrations from bead z-stack calibration. (b) Full FOV image reconstructed using Vectorfit and fitted aberrations from single molecules. (c) and (d) insets of (b), where (i) shows vector fitting and (ii) Gaussian fitting by Picasso [27]. (e) Estimated Zernike aberration surfaces from single molecules of 3D data, compared to interpolated aberrations from bead z-stack calibration. (f) Full 3D FOV image reconstructed using Vectorfit and fitted aberrations from single molecules. The 3D image is shifted 14 µm to the upper right compared to the 2D image. The false color indicates the axial distance from the nominal focus. In the 3D image, the microtubules that overlay the nucleus are visible in blue, while in the 2D image, these regions appear black, as the emitters are too much out of focus. (g) and (h) insets of (f), where (i) shows the Vectorfit result and (ii) with SMAP [28]. (i) and (j) yz cross sections of the regions indicated in (g) and (h). Scale bars: 10 µm (b), (f), 500 nm (c), (d), (g), (h), (i), and (j).
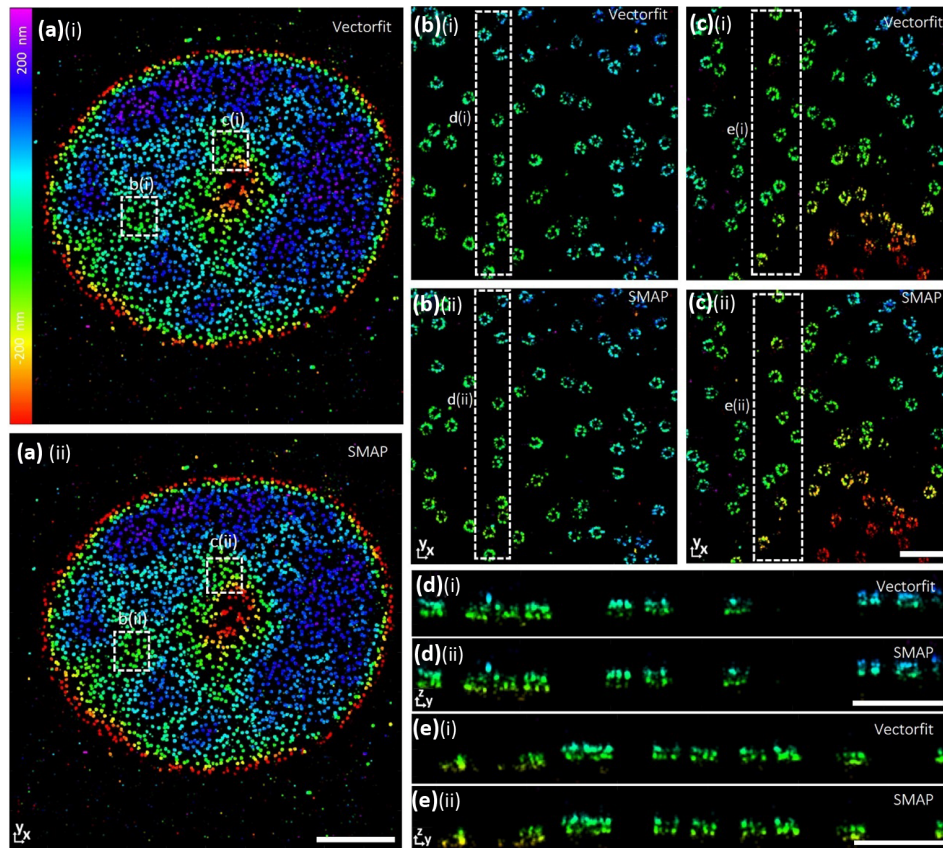
Fig. 3. Reconstructions for experimental 3D astigmatic data of NPCs. (a) (i)–(ii) Full FOV images reconstructed using Vectorfit with fitted aberrations from the single-molecule data, and SMAP using a spline PSF obtained from 3D bead calibration. (b) (i)–(ii) Zoomed views of the regions indicated by the boxes (b) (i)–(ii) in (a). (c) (i)–(ii) Zoomed views of the regions indicated by the boxes (c) (i)–(ii) in (a). (d) (i)–(ii) yz cross sections of the regions indicated by the boxes (d) (i)–(ii) in (b). (e) (i)–(ii) yz cross sections of the regions indicated by the boxes (e) (i)–(ii) in (c). Scale bars: 5 µm (a), 500 nm (b)–(e).

dataset, where NUP96 is labeled inside the NPC in U2OS cells over a 25×26 µm FOV [32]. In Fig. 3, we show that Vectorfit achieves comparable image quality as the reference processing via SMAP. The two NPC rings are clearly separated with Vectorfit, indicating that our method works for such challenging experimental samples. The linking analysis gives an average localization precision of 3.6 nm (xy) and 8.0 nm (z), with a CRLB of 2.9 nm (xy) and 7.0 nm (z), improving over the precision of 4.8 nm (xy) and 9.2 nm (z) for SMAP.

Next, we applied our method to another 3D dataset of NUP96 in the nuclear pore complex (NPC) of U2OS cells (FOV of about 180×180 µm) of Fu *et al.* [18], where the axial direction was encoded using astigmatism, and compared the outcome to that of their method, FD-DeepLoc, in Fig. 3. The aberration maps retrieved from the single-molecule data match well with the aberration maps obtained from the bead calibration used in FD-DeepLoc [see Fig. 5(a) and Figure S7 in Supplement 1], toward the edges of the FOV; however, the bead-calibration-derived aberration maps show large and erratic variations, which is unlikely from the point of view of NAT, which predicts field dependency by low-order polynomials. Figure 3(b) shows the experimentally found standard deviation for the estimation of the different aberrations, obtained from 30 estimations for different randomly selected subsets of 5000 localizations, as well as their Cramér–Rao lower bound (CRLB) values (see Section 2.4 in Supplement 1). The experimental standard deviations are on the small $m\lambda$ scale across the whole FOV, but do not reach the CRLB values in the sub-$m\lambda$ level. We

also tested the dependence of the experimental precision on the number of localization events M_s and found a scaling inversely proportional to $M_s^{1/2}$, in agreement with expectations (Figs. S8 and S9 in Supplement 1). The comparison of the modeled PSF to the measured single molecule spots in 4×4 patches across the FOV, as a function of the axial position (Visualization 2), shows a good match between the modeled PSF and the measured data. These validation tests indicate that our approach enables unbiased and precise aberration estimation.

We compared the Vectorfit reconstruction with field-dependent aberrations retrieved from the single-molecule data to a reconstruction with Vectorfit without aberrations, where all the aberrations are set to zero, except for a constant amount of astigmatism ($A_{22} = 103$ mλ, in accordance with the reported RMS value from the cylindrical lens) for estimating the axial location, and to the FD-DeepLoc reconstruction. In the center of the FOV, close to the optical axis, the reconstructions from the three methods are comparable (Figure S10 in Supplement 1). Toward the edges of the FOV, however, the aberrations become larger, leading to sizeable differences in the axial localization [see Figs. 3(c)–3(f)]. In one corner of the FOV, the FD-DeepLoc reconstruction shows a large spread of z locations within a single-cell nucleus [Fig. 4d(iii)]. The yz cross section in Fig. 4f(iii) shows a large variation of z locations in a single NPC, which seems unrealistic. In our reconstructions [Figs. 4d(i-ii) and 4f(i-ii)], the range of z locations matches much better with the expected thickness of the NPC ring of around 50 nm [31,33]. At the top
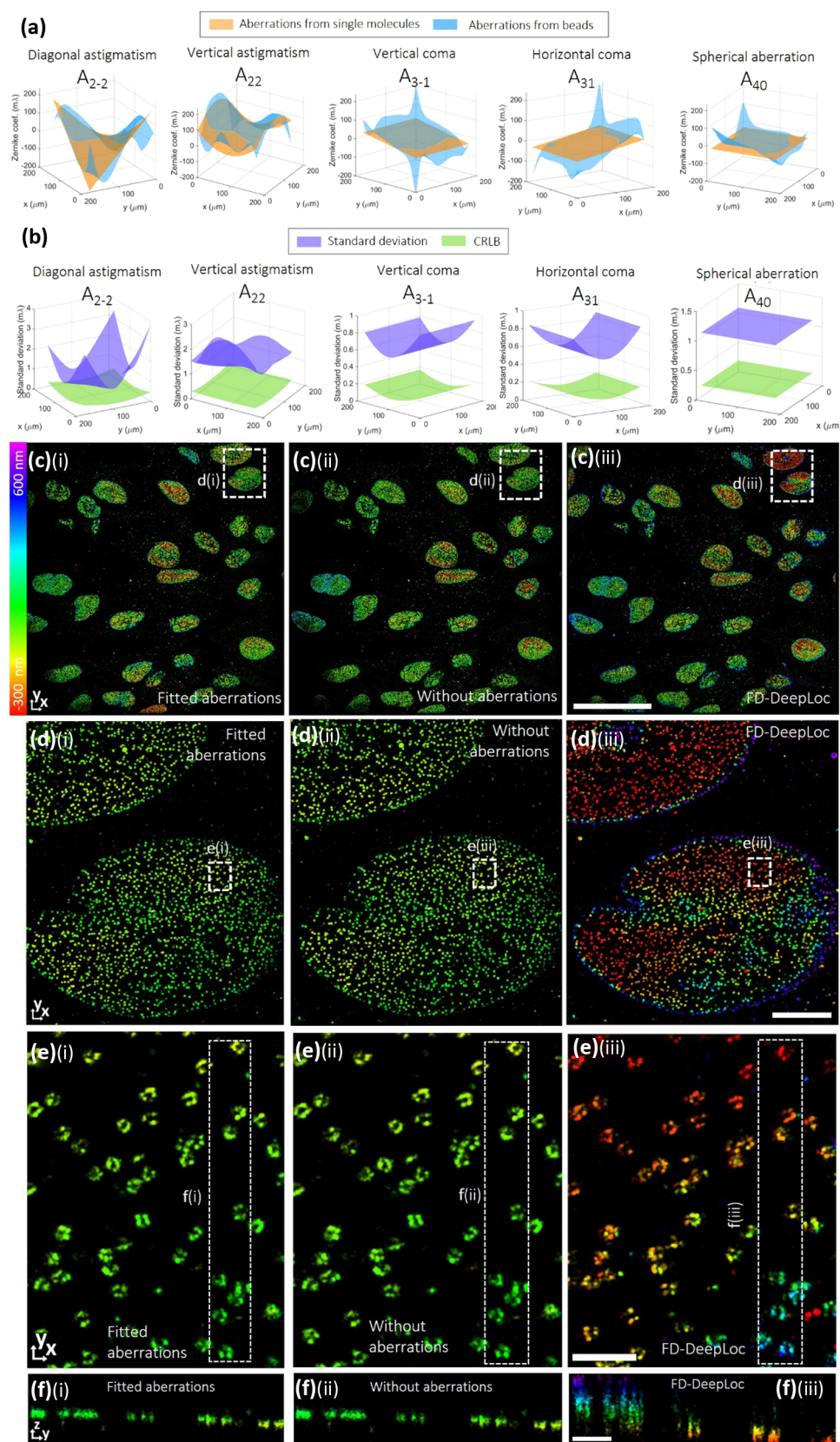
Fig. 4. Aberration estimation and reconstructions for experimental 3D astigmatic data of NPCs. (a) Estimated Zernike aberration surfaces from single molecules, compared to interpolated aberrations from bead *z*-stack calibration. (b) Standard deviation and CRLB for the estimated Zernike coefficients. The standard deviations were calculated by repeating the estimation process 30 times with different randomly selected subsets of 5,000 localizations. (c) (i)–(iii) Full FOV images reconstructed using fitted aberrations from single molecules, without aberrations ($A_{22} = 103$ mλ and other Zernike modes set to zero) and FD-DeepLoc. (d) (i)–(iii) Zoomed views of the regions indicated by the boxes (d) (i)–(iii) in (c). (e) (i)–(iii) Zoomed views of the regions indicated by the boxes (e) (i)–(iii) in (d). (f) (i)–(iii) *yz* cross sections of the regions indicated by the boxes (f) (i)–(iii) in (e). Scale bars: 50 µm (c), 5 µm (d), 500 nm (e), (f).
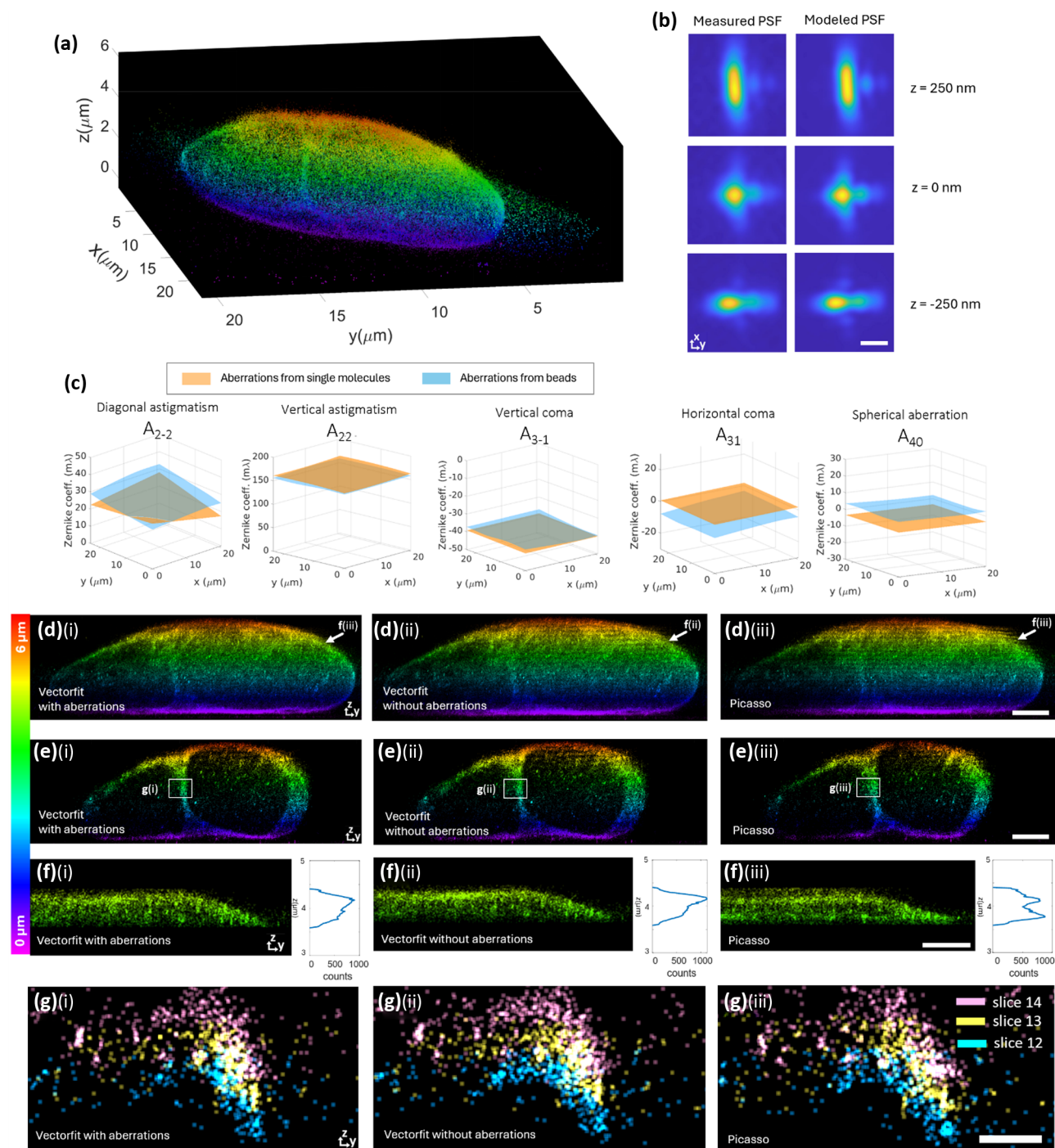
Fig. 5. Aberration estimation and reconstruction for experimental 3D astigmatic data of nuclear lamina. (a) Full cell nucleus reconstructed from multiple partially overlapping stage-shifted acquisitions using Vectorfit with field-dependent aberrations, where the color indicates the z value corresponding to the colorbar at (d), (e), and (f). (b) Average measured and modeled PSFs at different z values relative to the focal plane at $z = 0$. A total number of 51,922 ROIs, 75,767 ROIs, and 65,651 ROIs were averaged in a range of 100 nm centered around $z = -250$, $z = 0$, and $z = 250$ nm, respectively, and upsampled by a factor 10. (c) Estimated aberration surfaces from single-molecule data compared to interpolated aberrations from z-stack bead data. (d) xz projection of the nucleus over the full x range for (i) Vectorfit with field-dependent aberrations, (ii) Vectorfit without aberrations (only a constant amount of astigmatism $A_{22} = 163$ mλ), and (iii) Gaussian fitting with Picasso using a calibration curve obtained from the bead data for z-estimation. (e) The same as (d), but for a 1 μm thick slice in the x direction with x between 14.7 and 15.7 μm. (f) Same as (d), but only one yz slice at the position indicated in (d) and localization histogram as a function of axial position. (g) same as (e), zoom in at an invagination of the nuclear lamin. The localizations of three subsequent axial acquisitions, stage-shifted 250 nm, color coded. [Scale bars: 500 nm (b), 2 μm (d,e), 1 μm (f), and 500 nm (g)].

of the FOV, we observe that Vectorfit with field-dependent aberrations leads to a better reconstruction than without aberrations (Figure S11 in Supplement 1). A chi-square goodness-of-fit test

(Figure S12 in Supplement 1) shows that the Vectorfit model with field-dependent aberrations outperforms Vectorfit with constant aberrations, with a chi-square ratio reaching 1.5 at the edges of the

FOV. We also observe a shift in the lateral localizations of up to a few tens of nanometers (Figure S12b in Supplement 1) and a shift in the axial localizations of up to 150 nanometers (Figure S12c in Supplement 1). The distribution of localization precision values, estimated using the method of linking localizations in consecutive frames, has a mean of 11.7 nm (xy) and 23.5 nm (z) for Vectorfit with field-dependent aberrations, with a CRLB of 10.1 nm (xy) and 20.6 nm (z). For FD-Deeploc, we find by the same method a localization precision of 7.9 nm (xy) and 23.2 nm (z). With Vectorfit, we achieve the CRLB and therefore attain the optimal localization precision based on the signal-to-noise ratio of the data. The axial localization precision of Vectorfit is comparable to FD-Deeploc, but the lateral localization precision is a bit worse. We speculate that the learning-based approach of FD-Deeploc could bias localizations from the same emitter, which would introduce spurious correlations in subsequent time frames, resulting in a lower measured lateral localization precision than the CRLB. Analysis of the image resolution in a grid of 4×4 patches across the FOV with FRC thus shows slightly better image resolution for FD-DeepLoc than for VectorFit (Figure S13 in Supplement 1).

So far, we have applied first-order NAT, i.e., taking only primary astigmatism, coma, and spherical aberration into account, where the field dependence of the Zernike coefficients is described with low-order polynomials compatible with the aberration order. We have also made a fit of the NPC dataset using second-order NAT, which takes into account second-order astigmatism, coma, and spherical aberration, and primary trefoil, as well as higher-order polynomials for the dependence of Zernike coefficients on field coordinates (see Section 2 in Supplement 1). Figure S14 shows the result of the second-order NAT fit. It turns out that the 43 extra NAT coefficients can be fitted quite well. The fit converges within a few minutes, as the computational time scales linearly with the number of NAT coefficients. The values found for the 13 original first-order NAT coefficients were not very different from the values found in the first-order fit, resulting in Zernike coefficient maps across the FOV that are quite consistent with the first-order NAT maps (Figure S14a in Supplement 1) and with the aberrations estimated from bead z-stack calibration (Figure S14b in Supplement 1). Differences between the first- and second-order aberration surfaces do occur near the edge of the FOV, leading to small changes in the estimated locations (Fig. S15a-g in Supplement 1). The overall localization precision, derived from linking localizations in consecutive frames, improved a bit to 10.7 nm (xy) and 21.3 nm (z), with a CRLB of 10.2 nm (xy) and 21.0 nm (z). The average ratio of the chi-square values relative to the shot noise reference value decreased from 1.09 to 1.07 (Fig. S15h in Supplement 1), indicating an improvement in fit quality.

Finally, we applied our method to 3D astigmatic data of nuclear lamin A/C in a HeLa cell, imaging an entire nucleus [Fig. 5(a)] over a z-range of approximately 6 µm. This was achieved by measuring 22 z-stacks where the sample stage was moved 250 nm between each measurement (see Section 1 in Supplement 1 for experimental details). The aberrations estimated from the single-molecule data closely match the aberration maps obtained by interpolation between aberrations estimated from z-stack bead data [see Figs. 5(c) and Fig. S16 in Supplement 1], showing that the aberrations are dominated by constant amounts of vertical astigmatism and vertical coma. Additionally, averaging the measured single-molecule spots at different positions through focus [Fig. 5(b)] also

shows a PSF dominated by these two aberrations. The measured and modeled PSFs are very similar, confirming that our model accurately fits the data.

We compared the reconstruction using Vectorfit with field-dependent aberrations to a reconstruction using Vectorfit without aberrations, where all Zernike coefficients were set to zero, except for a constant amount of astigmatism ($A_{22} = 163$ mλ, equal to the average amount estimated from the bead data). Additionally, we compared the Vectorfit results to a reconstruction using Gaussian PSF fitting in Picasso [27] using a calibration curve for z-estimation obtained from the bead data. Figure 5(d) shows an xz projection of the fully reconstructed nucleus, while Fig. 5(e) shows an xz projection of a 1 µm thick slice in the y direction for all three methods. The reconstructions using Picasso exhibit a horizontal striping artifact and a serrated membrane edge that are significantly reduced when using Vectorfit and even more suppressed when taking into account field-dependent aberrations. Figure 5(e) shows a nuclear lamin invagination extending through the nucleus, which is narrower when using Vectorfit with field-dependent aberrations. In Fig. 5(f), we compare the reconstructions of one z-stack with the three reconstruction methods and investigated the axial localization histogram. By comparing the Vectorfit results of Fig. 5f(i,ii) to the Gaussian fit result of Fig. 5f(iii), we observe that in the latter case, the localizations are grouped into two axially separated batches. This gives rise to the striping observed in Figs. 5(e) and 5(d). The reason for this lies in the small amount of vertical coma that biases the Gaussian estimate, which relies on the ratio of the two fitted widths of a bivariate Gaussian [13]. This ratio is then compared against a modeled bead calibration curve obtained earlier to find the axial position. In Fig. 5(g), we compare the localizations of three subsequent stage-shifted acquisitions of the nuclear lamin invagination. In case the field-dependent aberrations are not included, the localizations [Fig. 5g(ii, iii)] are laterally displaced depending on the axial position, up to several hundred nanometers, giving rise to a bending artifact of the largely vertical line feature. In contrast, Vectorfit, including aberrations, does not give rise to such a shape distortion [Fig. 5f(i)]. The root cause of the bending artifact lies in the coma aberration, which we also see in a simulation study (see Fig. S17 in Supplement 1).

4. DISCUSSION

Fully vectorial PSF fitting in a maximum likelihood estimation (MLE) framework has not found its way into the practice of the SMLM field up to now. Software fitting is mostly dominated by the fitting of Gaussians or spline-based models. The reason is solely that the fitting speed was too slow for the typical number of localizations ($\sim 10^6$) in a super-resolution acquisition. CPU implementations of 2D Gaussian MLE fitting achieve currently about 10^4 fits/s and GPU implementations even more than 10^6 fits/s (7×7 pixel ROI). Only the phasor-based approach is equally quick on the CPU [25]. Our OTF-based algorithmic improvements for the fitting together with a high-end GPU (Nvidia A100) now allow 10^5 fits/s (see Table S1 in Supplement 1), while a good desktop GPU (Nvidia RTX A4000) has $6 \cdot 10^4$ fits/s, and a multi-core CPU still achieves $9 \cdot 10^3$ fits/s. This brings vectorial PSF fitting times for a typical dataset to less than a minute on a GPU in 2D. In 3D, our algorithmic improvements are less effective (for details, see Section 1 in Supplement 1), which results in $6.8 \cdot 10^3$ fits/s for a 17×17 pixel ROI on our desktop GPU which is about $30\times$ slower than 3D spline-based

fitting that achieves $2 \cdot 10^5$ fits/s on a desktop GPU for a 17×17 pixel ROI [34], but better than the less than 1 fit/s reported for a $17 \times 17 \times 41$ pixel bead stack [18].

Our approach of estimating aberrations directly from single-molecule data makes taking the inclusion of field-dependent aberrations to the localization much more feasible because it saves doing an additional bead calibration experiment, which can also be prone to errors as shown above. The recently proposed method from Liu *et al.* to estimate aberrations from single-molecule data can take more than half an hour on a GPU [21], while our model-based approach takes less than a minute on a CPU to estimate aberrations. In addition, our work is applicable to 2D localization data, while theirs is not. In 2D, however, the effect of field-dependent aberrations on the localizations is less impactful than in 3D.

The current practice in the field for 3D SMLM is astigmatic imaging followed by analysis via a bivariate Gaussian model [13,27]. We have shown in Fig. 5 that this analysis is prone to localization biases of several hundred nanometers even if relatively small amounts of coma are present of about half-Marechal's tolerance criterion (72 mλ). In practice, this limits the trusted axial range of imaging to about ± 200 nm around the focal plane instead of ± 500 nm, which should be possible theoretically. Using Vectorfit, including aberrations, we come close to this range, thereby allowing faithful structural 3D imaging. Rejecting all localization far from the focal plane could solve the structural deformation, but at the cost of a required finer axial sample. Vectorfit thus allows for twice as fast volumetric imaging compared to the current practice. Moreover, since coma can depend on position in the FOV, taking into account the field dependence of aberrations makes this possible for laterally extended FOVs.

In future work, a user interface should be developed to make vectorial PSF fitting accessible to a broader audience. Furthermore, the NAT-driven approach of estimating field-dependent aberrations directly from single-molecule data could be applied to other imaging modalities, such as 4Pi SMLM or localization microscopy with fixed dipole emitters, and also for scanning but camera-based localization microscopy [35].

Disclosures. The authors declare no conflicts of interest.

Data availability. Code and a software demo are available at Ref. [24].

Supplemental document. See Supplement 1 for supporting content.

REFERENCES

1. E. Betzig, G. H. Patterson, R. Sougrat, *et al.*, "Imaging intracellular fluorescent proteins at nanometer resolution," Science **313**, 1642–1645 (2006).
2. M. J. Rust, M. Bates, and X. Zhuang, "Sub-diffraction-limit imaging by stochastic optical reconstruction microscopy (STORM)," Nat. Methods **3**, 793–796 (2006).
3. A. Sharonov and R. M. Hochstrasser, "Wide-field subdiffraction imaging by accumulated binding of diffusing probes," Proc. Natl. Acad. Sci. USA **103**, 18911–18916 (2006).
4. M. Heilemann, S. van de Linde, M. Schüttpelz, *et al.*, "Subdiffraction-resolution fluorescence imaging with conventional fluorescent probes," Angew. Chem. **47**, 6172–6176 (2008).
5. K. M. Douglass, C. M. Sieben, A. Archetti, *et al.*, "Super-resolution imaging of multiple cells by optimized flat-field epi-illumination," Nat. Photonics **10**, 705–708 (2016).
6. J. Deschamps, A. Rowald, and J. Ries, "Efficient homogeneous illumination and optical sectioning for quantitative single-molecule localization microscopy," Opt. Express **24**, 28080–28090 (2016).
7. R. Diekmann, Ø. I. Helle, C. I. Øie, *et al.*, "Chip-based wide field-of-view nanoscopy," Nat. Photonics **11**, 322–328 (2017).
8. A. Archetti, E. Glushkov, C. Sieben, *et al.*, "Waveguide-PAINT offers an open platform for large field-of-view super-resolution imaging," Nat. Commun. **10**, 1267 (2019).
9. A. Mau, K. Friedl, C. Leterrier, *et al.*, "Fast widefield scan provides tunable and uniform illumination optimizing super-resolution microscopy on large fields," Nat. Commun. **12**, 3077 (2021).
10. Q. Li, C. N. Hulleman, R. J. Moerland, *et al.*, "Waveguide-based total internal reflection fluorescence microscope enabling cellular imaging under cryogenic conditions," Opt. Express **29**, 34097–34108 (2021).
11. H. Ma, M. Chen, P. Nguyen, *et al.*, "Toward drift-free high-throughput nanoscopy through adaptive intersection maximization," Sci. Adv. **10**, eadm7765 (2024).
12. T. Nelson, S. Vargas-Hernández, M. Freire, *et al.*, "Multimodal illumination platform for 3D single-molecule super-resolution imaging throughout mammalian cells," Biomed. Opt. Express **15**, 3050–3063 (2024).
13. C. S. Smith, N. Joseph, B. Rieger, *et al.*, "Fast, single-molecule localization that achieves theoretically minimum uncertainty," Nat. Methods **7**, 373–375 (2010).
14. S. Stallinga and B. Rieger, "Accuracy of the Gaussian point spread function model in 2D localization microscopy," Opt. Express **18**, 24461–24476 (2010).
15. R. Ø. Thorsen, C. N. Hulleman, M. Hammer, *et al.*, "Impact of optical aberrations on axial position determination by photometry," Nat. Methods **15**, 989–990 (2018).
16. Y. Li, M. Mund, P. Hoess, *et al.*, "Real-time 3D single molecule localization using experimental point spread functions," Nat. Methods **15**, 367–369 (2018).
17. C. N. Hulleman, R. Ø. Thorsen, E. Kim, *et al.*, "Simultaneous orientation and 3D localization microscopy with a Vortex point spread function," Nat. Commun. **12**, 5934 (2021).
18. S. Fu, W. Shi, T. Luo, *et al.*, "Field-dependent deep learning enables high-throughput whole-cell 3D super-resolution imaging," Nat. Methods **20**, 459–468 (2023).
19. L. von Diezmann, M. Y. Lee, M. D. Lew, *et al.*, "Correcting field-dependent aberrations with nanoscale accuracy in three-dimensional single-molecule localization microscopy," Optica. **2**, 985–993 (2015).
20. F. Xu, D. Ma, K. P. MacPherson, *et al.*, "Three-dimensional nanoscopy of whole cells and tissues with in situ point spread function retrieval," Nat. Methods **17**, 531–540 (2020).
21. S. Liu, J. Chen, J. Hellgoth, *et al.*, "Universal inverse modeling of point spread functions for SMLM localization and microscope characterization," Nat. Methods **21**, 1082–1093 (2024).
22. R. V. Shack and K. Thompson, "Influence of alignment errors of a telescope system on its aberration field," Proc. SPIE **0251**, 146–153 (1980).
23. M. Bates, J. Keller-Findeisen, A. Przybylski, *et al.*, "Optimal precision and accuracy in 4Pi-STORM using dynamic spline PSF models," Nat. Methods **19**, 603–612 (2022).
24. I. Droste, E. Schuitema, S. A. Khan, *et al.*, "Vectorfit," GitLab, 2025, https://gitlab.tudelft.nl/imphys/ci/vectorfit.
25. K. Martens, A. N. Bader, S. Baas, *et al.*, "Phasor based single-molecule localization microscopy in 3D (pSMLM-3D): an algorithm for MHz localization rates using standard CPUs," J. Chem. Phys. **148**, 123311 (2018).

26. M. Siemons, C. N. Hulleman, R. Ø. Thorsen, *et al.*, "High precision wave-front control in point spread function engineering for single emitter localization," Opt. Express **26**, 8397–8416 (2018).

27. I. Droste, E. Schuitema, S. A. Khan, *et al.*, "Super-resolution microscopy with DNA-PAINT," Nat. Protocols **12**, 1198–1228 (2017), https://github.com/jungmannlab/picasso.

28. J. Ries, "SMAP: a modular super-resolution microscopy analysis platform for SMLM data," Nat. Methods **17**, 870–872 (2020).

29. J. Cnossen, T. Hinsdale, R. Ø. Thorsen, *et al.*, "Localization microscopy at doubled precision with patterned illumination," Nat. Methods **17**, 59–63 (2020).

30. R. P. J. Nieuwenhuizen, K. A. Lidke, M. Bates, *et al.*, "Measuring image resolution in optical nanoscopy," Nat. Methods **10**, 557–562 (2013).

31. J. V. Thevathasan, M. Kahnwald, K. Cieslinski, *et al.*, "Nuclear pores as versatile reference standards for quantitative superresolution microscopy," Nat. Methods **16**, 1045–1053 (2019).

32. Y. L. Wu, P. Hoess, A. Tschanz, *et al.*, "Maximum-likelihood model fitting for quantitative analysis of SMLM data," Nat. Methods **20**, 139–148 (2023).

33. W. Wang, A. Jakobi, Y.-L. Wu, *et al.*, "Particle fusion of super-resolution data reveals the unit structure of Nup96 in nuclear pore complex," Sci. Rep. **13**, 13327 (2023).

34. M. Li, W. Shi, S. Liu, *et al.*, "Fast and universal single-molecule localization using multi-dimensional point spread functions," Opt. Express **32**, 42601–42615 (2024).

35. N. Radmacher, O. Nevskyi, J. Ignacio Gallea, *et al.*, "Doubling the resolution of fluorescence-lifetime single-molecule localization microscopy with image scanning microscopy," Nat. Photonics **18**, 1059–1066 (2024).